

# Repeating caldera collapse events constrain fault friction at the kilometer scale

Paul Segall<sup>a,1</sup> and Kyle Anderson<sup>b</sup>

<sup>a</sup>Geophysics Department, Stanford University, Stanford, CA 94305; and <sup>b</sup>US Geological Survey, Volcano Science Center, Moffett Field, CA 94035

Edited by James H. Dieterich, University of California, Riverside, CA, and approved June 16, 2021 (received for review January 23, 2021)

Fault friction is central to understanding earthquakes, yet laboratory rock mechanics experiments are restricted to, at most, meter scale. Questions thus remain as to the applicability of measured frictional properties to faulting in situ. In particular, the slip-weakening distance  $d_c$  strongly influences precursory slip during earthquake nucleation, but scales with fault roughness and is challenging to extrapolate to nature. The 2018 eruption of Kīlauea volcano, Hawaii, caused 62 repeatable collapse events in which the summit caldera dropped several meters, accompanied by  $M_W$  4.7 to 5.4 very long period (VLP) earthquakes. Collapses were exceptionally well recorded by global positioning system (GPS) and tilt instruments and represent unique natural kilometerscale friction experiments. We model a piston collapsing into a magma reservoir. Pressure at the piston base and shear stress on its margin, governed by rate and state friction, balance its weight. Downward motion of the piston compresses the underlying magma, driving flow to the eruption. Monte Carlo estimation of unknowns validates laboratory friction parameters at the kilometer scale, including the magnitude of steady-state velocity weakening. The absence of accelerating precollapse deformation constrains  $d_c$  to be  $\leq$ 10 mm, potentially much less. These results support the use of laboratory friction laws and parameters for modeling earthquakes. We identify initial conditions and material and magma-system parameters that lead to episodic caldera collapse, revealing that small differences in eruptive vent elevation can lead to major differences in eruption volume and duration. Most historical basaltic caldera collapses were, at least partly, episodic, implying that the conditions for stick-slip derived here are commonly met in nature.

fault friction | caldera collapse | Kīlauea volcano

ur knowledge of rock friction comes from laboratory experiments on samples from centimeters to at most meter scale (1, 2). These experiments have led to rate- and state-dependent friction laws (3, 4), which together with continuum fault models explain many features of natural earthquakes (5, 6). Extrapolation of laboratory-derived constitutive parameters to faults in situ, however, has been challenging, particularly for the characteristic slip weakening distance,  $d_c$ , the displacement scale over which friction degrades from nominally static to dynamic values. In the laboratory  $d_c$  ranges from several to tens of micrometers, but scales with fault roughness (7). Some seismological estimates are up to five orders of magnitude larger (8), but are sensitive to the decrease in shear strength at earthquake rupture fronts, leading to weakening lengths that scale with  $d_c$ , but can be much larger (9, 10). Understanding the magnitude of  $d_c$  in situ is crucial because the amount of potentially observable precursory slip scales with  $d_c$  (11). Significant insights have been gained from in situ fluid injection experiments into faults that induce aseismic slip and seismicity (12-14), yet constraints on the parts of faults that actually generate earthquakes

Collapse at basaltic shield volcanoes typically occurs in repeated discrete events, generating characteristic deformation transients and very long period (VLP) earthquakes (15-17). Rapid outflow of magma causes the pressure in subcaldera

magma reservoirs to decrease, leading to an increase in stress in the overlying crust. Collapse initiates if this stress reaches the crustal strength, forming ring faults bounding down-dropped block(s) (18). Once initiated, collapse transfers the weight of the overlying crust onto the magma reservoir, maintaining pressure necessary for the eruption to continue (19). Thus, caldera collapse is not simply a response to the rapid withdrawal of magma, but is also an essential process in sustaining these eruptions.

The 2018 Kīlauea collapses were quasi-periodic and exceptionally well monitored by nearby global positioning system (GPS) and tilt stations, including GPS stations on the downdropped block(s). These data can be used to infer stress changes on the caldera-bounding ring faults, making them effectively kilometer-scale stick-slip experiments. The highly repeatable nature of the collapses, as well as constraints on the changes in magma pressure prior to the onset of collapse (20), minimizes uncertainty due to otherwise difficult to constrain initial conditions.

#### Results

The eruption began on 3 May 2018 in Kīlauea's lower East Rift Zone, 40 km from the summit caldera (21). Deflationary deformation (inward and downward displacements) measured by GPS, tilt, and Interferometric Synthetic Aperture Radar (InSAR) satellites in early May constrained the subcaldera (Halema'uma'u) magma reservoir to be centered ~2 km beneath the surface with a volume of 2.5 to 7.2 km<sup>3</sup> (68% bounds) (20). Discrete collapse events began in mid-May and by the end of the month surface faulting extended outside the Halema'uma'u

## **Significance**

Earthquake physics require understanding how the frictional resistance on faults varies leading up to and during seismic slip. Laboratory rock friction experiments have led to widely used friction laws that depend on sliding rate and slip history. However, these experiments are restricted to samples vastly smaller than natural faults. Highly repeatable, and exceptionally well instrumented, caldera collapse events at Kīlauea volcano can be treated as kilometer-scale rock friction experiments and entirely validate laboratory experiments. Caldera collapse is caused by rapid draining of magma from a shallow crustal reservoir. Collapse transfers weight to the underlying magma reservoir, thereby sustaining the eruption. Our results permit more accurate understanding of conditions leading to caldera collapse and high-rate basaltic eruptions.

Author contributions: P.S. designed research; P.S. and K.A. performed research; K.A. analyzed data; and P.S. wrote the paper.

The authors declare no competing interest.

This article is a PNAS Direct Submission.

Published under the PNAS license.

<sup>1</sup>To whom correspondence may be addressed. Email: segall@stanford.edu.

This article contains supporting information online at https://www.pnas.org/lookup/suppl/ doi:10.1073/pnas.2101469118/-/DCSupplemental.

Published July 23, 2021.

crater. A new fault scarp propagated through the preexisting Kīlauea caldera, associated with volcano-tectonic seismicity (22), establishing a roughly circular collapse structure by mid-tolate June 2018. We focus on the final 32 collapse events, with average repeat times of  $1.4 \pm 0.3$  d, that followed formation of this structure. GPS station CALS located near the eastern edge of the down-dropped block abruptly subsided  $2.4 \pm 0.3$  m per event (Fig. 1). However, there was also  $\sim$ 2 m of gradual intercollapse subsidence at CALS (Fig. 1A), which because of its proximity to the ring fault may not reflect the larger collapse structure. Differences between digital elevation models permit as much as 5 m of subsidence per collapse cycle, but cannot resolve how much of this occurred abruptly during the collapse events (21, 23). We therefore take the collapse displacement to be uniformly distributed between 2.4 and 5.0 m with Gaussian tails with standard deviation of 0.2 m. The final 32 collapses lasted 5 to 10 s based on 5-s sampled GPS data from nearby stations. We take the duration to be uniformly distributed between 5 and 10 s with 1-s Gaussian tails.

GPS and tilt stations located outside of the growing caldera exhibited rapid inflation (upward and outward deformations) coincident with collapse at intracaldera sites, followed by a decaying deflationary signal (Fig. 1A). Following a rapid shortduration decay, GPS radial displacements exhibit an exponential decay with a time constant  $0.5 \pm 0.1$  d (Fig. 1C). Cocollapse deformation was principally caused by compression of the magma reservoir induced by collapse of the overlying rock, although slip on the ring faults may have contributed (23). The ring faults are inward dipping at the surface; GPS displacements are consistent with them steepening to vertical at a few hundred meters depth. The pressure increase during collapse,  $\Delta p$ , for vertical ring faults, conditioned both on cocollapse GPS displacements and on precollapse results for magma chamber volume and compressibility, is  $3 \pm 0.3$  MPa (23). The pressure increment  $\Delta p$  is a proxy for the inflationary GPS deformation shown in Fig. 1 A and B. Results are not substantially different for steeply dipping normal faults; we do, however, increase the uncertainty slightly to account for variable dip. The observations used to constrain frictional and magma chamber properties are summarized in Table 1.

Consider a cylindrical caldera block (piston) of radius R, height L, and density  $\rho_c$  (Fig. 2). Pressure p at the base of the

block and shear stress  $\tau$  on its margin balance its weight, such that momentum balance (on a per area basis) is

$$\frac{R\rho_c g}{2} - \frac{R}{2L}p(t) - \tau(t) = \frac{R\rho_c}{2}\frac{dv}{dt},$$
 [1]

where v is the downward velocity of the block.

The change of mass within the magma reservoir is balanced by mass flux to the eruption. The flux is assumed proportional to the chamber pressure in excess of the magmastatic head,  $p-p_e-\rho gu$ , where  $p_e=\rho g(L-\Delta h)$  and  $\Delta h$  is the initial height difference between the caldera and the eruption (Fig. 2). The term  $\rho gu$  accounts for the loss of pressure as the block displaces downward by amount u. Thus,

$$\frac{dp}{dt} = -\frac{k}{\rho \bar{\beta}(t) V(t)} \left[ p(t) - p_e - \rho g u(t) \right] + \frac{\pi R^2}{\bar{\beta}(t) V(t)} v(t), \quad [2]$$

where k depends on the conduit dimensions and melt viscosity, and  $\rho, \bar{\beta}, V$  are magma density, the system compressibility (chamber plus magma), and chamber volume, respectively. The final term represents magma pressurization due to downward motion of the caldera block. Because outflow during the eruption was orders of magnitude greater than recharge rates (20), flow into the magma chamber is not included.

The system of equations is closed with du/dt = v, and a regularized form of rate- and state-dependent friction (24)

$$\tau = a\sigma \operatorname{arcsinh} \left\{ \frac{v}{2v^*} e^{f_0/a} \left( \frac{\theta v^*}{d_c} \right)^{b/a} \right\}$$
 [3]

$$\frac{d\theta}{dt} = -\frac{\theta v}{d_c} \log \left(\frac{\theta v}{d_c}\right),$$
 [4]

where  $\theta$  is the state variable,  $\sigma$  is effective normal stress,  $f_0, a, b$  are constitutive parameters,  $v^*$  is a normalizing constant, and  $d_c$  is the state evolution distance. For sufficiently large v the steady-state frictional resistance is  $\tau_{ss} = \sigma \left[ f_0 + (a-b) \log(v/v^*) \right]$ .

Our model builds on work of ref. 15 as well as refs. 17 and 25; however, ref. 15 assumed constant magma outflow, while ref. 17 did not include magma compressibility or potential for stick-slip. Most importantly, this study includes a

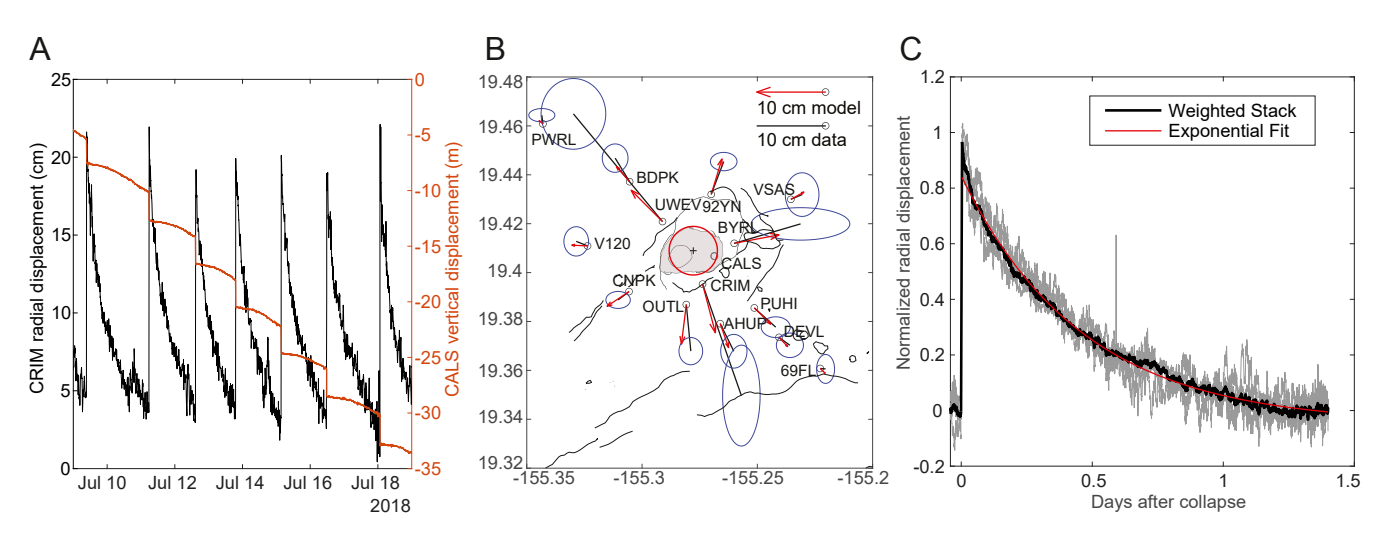


Fig. 1. (A) Time series of caldera-radial GPS displacement at CRIM and vertical displacement at CALS. Radial is positive away from the caldera. Station locations are shown in B. (B) Cocollapse horizontal displacements. Black vectors: average of last 32 events, with 95% confidence ellipses. Red vectors: predicted by model with 90° fault dip and magma compressibility  $\beta_m = 3 \times 10^{-10} \text{ Pa}^{-1}$  (23). Collapse structure is shaded. Red circle: model ring fault. (C) Weighted stack of radial GPS displacements for stations external to collapse. Gray curves show stations with offset over 40 mm. Red: exponential fit with decay time of 0.46 d.

Table 1. Observables and MAP model predictions

Observation	Mean value	Standard deviation	MAP prediction
Recurrence time, d	1.4	0.3	1.4
Duration, s	5 to 10 <sup>†</sup>	1.0	5.2
Pressure change, MPa	3.0	0.5	3.0
Displacement, m	$2.4 \text{ to } 5.0^{\dagger}$	0.2	3.5
Decay time, d	0.5	0.1	0.5

Most parameters are assumed normally distributed. MAP, maximum a posteriori model.

 $^{\dagger}\text{Uniform}$  over the given interval, with Gaussian tails at stated standard deviation.

laboratory-derived friction law capable of exhibiting stick-slip oscillations.\*

As magma flows to the eruption site the magma pressure acting on the piston decreases, thus increasing the shear stress on the ring fault (Fig. 2). Eventually the effective frictional strength is reached. As the piston descends the frictional resistance may weaken, causing the block to accelerate downward. Downward motion pressurizes the underlying magma, decelerating the block, eventually bringing it back into static equilibrium. Whether collapse occurs depends on the strength of the ring fault and the shear stresses acting there. Fault strength depends on the effective normal stress and nominal static friction coefficient. The shear stress depends on the precollapse state and the decrease in magma pressure.

The governing equations exhibit a rich variety of behaviors. Depending on parameter values and initial conditions, the system can 1) decay to magmastatic pressure, possibly following one or more collapse events; 2) evolve to a steady-state subsidence, either monotonically or via decaying noninertial oscillations (strictly steady state occurs only if the  $\rho gu$  term in Eq. 2 is neglected); or 3) produce a sequence of repeating stick–slip cycles.

We show in *Materials and Methods* that repeated stick–slip occurs only if 1) the friction is velocity weakening (b > a); 2) a steady-state solution to the quasi-static governing equations (ignoring changing chamber geometry and magmastatic head loss) exists, with plug velocity  $v_{ss}$ ; and 3) the state evolution distance is less than a critical value given by

$$(d_c)_{crit} = \sigma(b-a) \left[ \frac{\pi R^3}{2LV\bar{\beta}} + \frac{\sigma a}{v_{ss}t^*} \right]^{-1},$$
 [5]

where  $t^* = \rho \bar{\beta}_0 \, V_0/k$  is a characteristic pressure decay time. Our results distinguish initial conditions and ranges of material and magma system parameters that lead to episodic collapse. Note that the term with  $V\bar{\beta}$  plays a role similar to that of spring stiffness in the classic spring-slider model (3); as the block moves downward it compresses the underlying magma, increasing pressure so that less friction is required to maintain momentum balance. In this case the loading is due to time-dependent magma flow, rather than steady load-point motion.

Whether stick–slip oscillations occur and their characteristics are sensitive to friction and other system parameters. This suggests that observations in Table 1 can be used to constrain these parameters. As we focus on the character of the stick–slip events, not their evolution over the course of the eruption, we neglect changes in chamber volume and compressibility in these simulations; i.e.,  $V\bar{\beta}$  is kept at its initial value. For a few stick–slip cycles the change in volume is at most a few percent. We also

ignore the change in magmastatic head  $[\rho gu(t)]$  term in Eq. 2] which does not significantly influence behavior on the time scale of several stick–slip cycles.

The unknowns are the friction parameters,  $f_0$ , a, b,  $d_c$  and parameters that describe the magma chamber: V, L,  $\bar{\beta}$ , the pressure decay time  $t^*$ , and a normal stress correction factor  $\sigma_f$ . The a priori effective normal stress acting on the ring fault is lithostatic pressure (density  $2.5 \times 10^3 \text{ kg m}^{-3}$ ) minus hydrostatic pressure (water table depth taken to be 500 m). However, topographic stress and flank spreading (27, 28) could modify this value. We thus multiply the a priori average normal stress by a factor  $\sigma_f$ , permitted to range over [0.33, 1.5]. A priori bounds on model parameters are given in SI Appendix.

There are more unknowns than observables; however, the model is highly nonlinear and large parts of parameter space do not exhibit stick-slip. We use a Markov chain Monte Carlo routine with multiple parallel chains, randomly started from results of a preliminary run, to sample the posterior distribution of parameters consistent with these observations. The maximum a posteriori estimate (MAP) model (Fig. 3) fits the data very well (Table 1); however, we are primarily interested in the distribution of parameters consistent with the data and priors. Distributions for 2.2 million samples (acceptance rate 37.4%) are shown in Fig. 4. Also shown are a priori estimates of these parameters, subjected to the constraint that the parameters exhibit stick-slip cycles. The nominal friction coefficient  $f_0$ is bounded between 0.27 and 0.79 (95% bounds), although the distribution is skewed to values over 0.5. While the frictional direct effect a is not well resolved, b-a is resolved to between  $0.9 \times 10^{-3}$  and  $6.0 \times 10^{-3}$ . This is remarkably consistent with laboratory experiments (29) on basalt at 45 to 51 MPa effective normal stress and temperatures up to 600 °C. Zhang et al. (29) find friction coefficients in the range 0.7 to 0.74, slightly increasing with temperature. They further report rate-strengthening friction for temperatures less than 200 °C, but rate weakening in the range 300 to 600 °C. Laboratory-derived b-a ranges from 1 to  $6 \times 10^{-3}$ , depending on temperature and whether the slip or aging law is used to model the data, nicely overlapping the range of our kilometer-scale estimates.

For simulated gouge between saw-cut surfaces Zhang et al. (29) find  $d_c$  of a few to a few tens of micrometers. We find that  $d_c$  is less than 0.08 m at 98% confidence, although much smaller  $d_c$  also fits the data. Because decreasing  $d_c$  dramatically increases model run time without changing data fit, we restricted values to  $\geq 10^{-4}$  m. SI Appendix, Fig. 2 shows that over this range  $d_c$  is not strongly correlated with other parameters (with the slight exception of  $t^*$ ), suggesting that exclusion of smaller  $d_c$  does not bias other parameters. Importantly, values of  $d_c$  toward the upper end of the sample range predict substantial precollapse deformation that is not observed in the data (Fig. 4B). Thus,  $d_c$  must be less than 10 mm and is quite likely much less. The

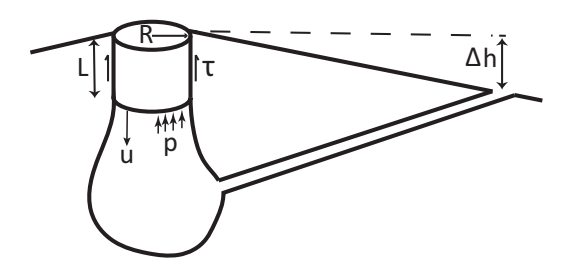


**Fig. 2.** A cylindrical caldera block of radius R and length L and density  $\rho_c$  is supported by pressure p at its base and shear stress  $\tau$  on its sides and undergoes downward displacement u. The underlying chamber with initial volume  $V_0$  contains magma with density  $\rho$ . The elevation difference between the top of the caldera block and the eruptive vent is  $\Delta h$ .

<sup>\*</sup>Ref. 26, published during revision of this paper, applies the model of ref. 15, with static–dynamic friction, including pressure-dependent outflow (17) to the 2018 Kilauea eruption.



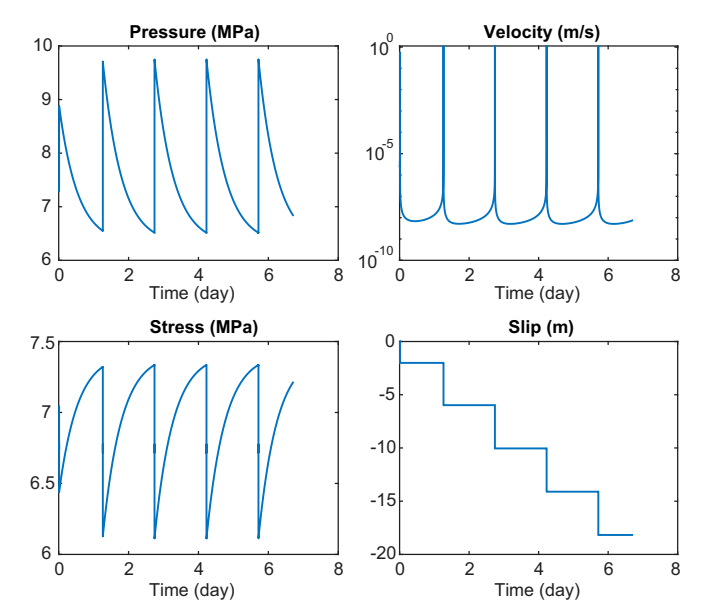


Fig. 3. Predicted pressure, slip velocity, shear stress, and piston displacement for the MAP model with  $d_{\rm c} \leq$  10 mm. Pressure is reckoned at the top of the magma chamber.

absence of accelerating, precollapse deformation is consistent with observations from other basaltic volcanoes (30).

Numerical simulations (31) show that slip-weakening length scales at rupture fronts can be 20 times the intrinsic  $d_c$ . Our upper bound on  $d_c$  is thus consistent with seismic estimates no greater than 0.2 m. Episodicity at nearly all observed basaltic collapses suggests that the conditions for stick-slip identified in Eq. 5 are commonly met in nature.

The slow subsidence at CALS, located on the caldera block, in the roughly half day prior to collapses (Fig. 1A) is highly correlated with volcano tectonic (VT) earthquakes, which are concentrated on the eastern sector of the collapse (22). These VT events do not clearly delineate a complete ring-fault structure, although they must also result from stressing due to magma withdrawal. Thus, while the CALS subsidence does precede collapse events, it appears to be distinct from accelerating slip on the ring fault as modeled in Fig. 4.

The effective frictional strength,  $\tau$ , equal to the maximum shear stress during stick-slip cycles, is crucial in determining whether collapse occurs. Relative to the prior,  $\tau$  is well resolved at 5.0 to 9.3 MPa (Fig. 4). In comparison, the increase in shear stress on the ring fault due to magma withdrawal at the time of the first collapse  $\Delta \tau$  was 5.5 to 14.9 MPa (20). The total stress at collapse onset is the sum of the stress change,  $\Delta \tau$ , and the preexisting shear stress,  $\tau_0$ . Collapses began before the ring fault had fully formed, requiring the formation of new faults. Because of cohesion, C, the strength of intact rock,  $\tau_f$ , is generally higher than for preexisting faults (32); near-vertical basalt cliffs imply cohesion of several megapascals (33). In addition, preexisting faults at Kīlauea may have healed since the previous collapse several centuries ago. For simplicity, we include this effect with cohesion. Thus,  $\tau_f = \tau + C = \tau_0 + \Delta \tau$ , or  $\tau =$  $\tau_0 + \Delta \tau - C$ . That the distributions on  $\tau$  and  $\Delta \tau$  largely overlap implies  $\tau_0 - C$  is relatively small, and perhaps slightly negative, although model/data limitations cannot be eliminated. Thus, while there are significant uncertainties, both studies imply the shear strength of the shallow (upper kilometer) crust is roughly 10 MPa.

### Discussion

The model explains the conditions necessary for collapse and thus high-volume rate basaltic eruptions. As discussed above, the sum of the initial shear stress and that induced by magma withdrawal must reach the static strength of the overlying crust. The upper bound on pressure drop is that which brings the pressure at the chamber outlet into static equilibrium with a column of magma to the eruption vent. Thus, for lower elevation eruptions the pressure can drop further before flow ceases (34), permitting a larger stress increase on the ring faults and a higher likelihood of collapse. This is illustrated in Fig. 5 with two solutions at different  $\Delta h$ , the height difference between the caldera floor and the eruptive vent; all other parameters are fixed. For  $\Delta h = 775$ m the pressure decays monotonically; the shear stress never reaches the threshold for unstable slip (35). For these parameters, if the eruptive vent is only 25 m lower, the pressure drops sufficiently to trigger a sequence of collapse events, leading to a prolonged eruption ( $\Delta h$  was  $\sim 800$  m in 2018). Lower-elevation eruptions are more likely to trigger caldera collapse and sustain a long-lived eruption.

Indeed, the 2007 Piton de la Fournaise eruption began at the volcano's summit, but collapse initiated only when the eruption

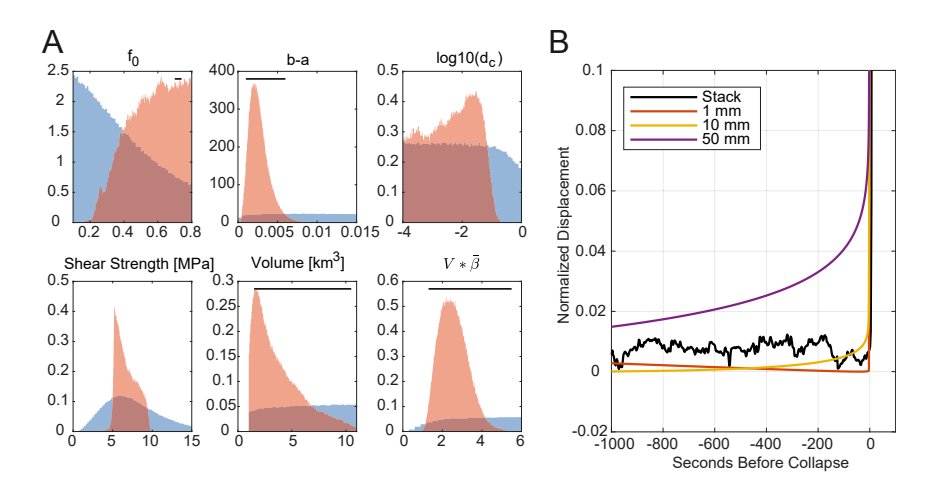


Fig. 4. (A) Posterior distributions based on 2.2 million samples (red) and a priori distributions conditional on the existence of linearly unstable steady-state solutions (blue). Black horizontal lines mark the range of values from Zhang et al. (29) for friction parameters and from Anderson et al. (20) for the magma chamber parameters. (B) Precollapse deformation. Data are from a weighted stack of GPS radial components external to the collapse. Model predictions are from scaled pressure time history for representative models with the specified  $d_c$ . External GPS stations respond primarily to pressure change in the shallow reservoir (23). Time is measured relative to the collapse event.

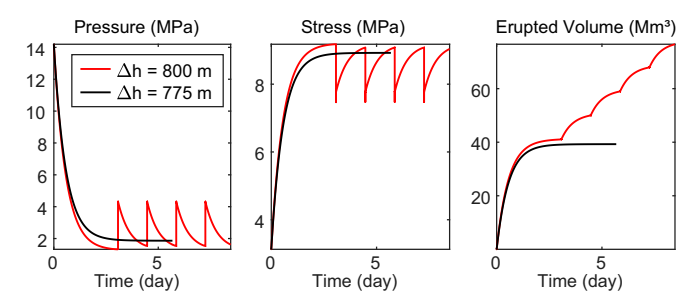


Fig. 5. Sensitivity of eruption behavior to difference in elevation between caldera block and eruptive vent  $\Delta h$ . All other parameters are held constant. Pressure is reckoned at the base of the collapse block (Fig. 2). Stress is average shear stress on the sides of the collapse block. Erupted volume is in million cubic meters and shows how collapses serve to maintain the eruption.

shifted 1,300 m lower (16). The summit of Bárarbunga, Iceland is over 1 km above the eruptive vents during the 2014 collapse (17), and the 2000 Miyakejima collapse was accompanied by a deep submarine dike intrusion (36). Kīlauea erupted for 35 y from the Pu'u'ō'ō vent—600 m higher than the 2018 vents—without causing caldera collapse. (In addition, eruption rates during the Pu'u'ō'ō phase were much lower than in 2018, allowing recharge from the mantle to sustain summit magma pressures). On the other hand, some previous low-elevation eruptions at Kīlauea did not cause collapse. As eruptions wane, heat loss increases magma viscosity, eventually leading to freezing. Thus, low-elevation eruptive vents are a necessary, but insufficient condition for basaltic caldera collapse; the size of the conduit leading to the vent and the resulting magma flux also play a critical role.

The volume of the subcaldera magma reservoir is constrained to 1.1 to 9.7 km<sup>3</sup>, limited by the prior lower bound. In comparison, Anderson et al. (20) constrain the volume of this reservoir to between 1.5 and 10.5 km<sup>3</sup>. The product of the magma reservoir volume and the net compressibility  $V\bar{\beta}$  is somewhat better resolved in this study (1.4 to 4.1 m<sup>3</sup>/Pa), compared to 1.3 to 5.5 m<sup>3</sup>/Pa from ref. 20. Of course, our results are not completely independent of ref. 20's results, as they informed our priors for chamber volume and compressibility.

There is considerable opportunity to extend our analysis. The lumped parameter model cannot describe the spatial evolution of ring-fault slip. Faults within a fully elastic domain must reach a critical nucleation dimension  $L_c = \pi G d_c / 4(b-a)\sigma$  before becoming dynamic, where G is the shear modulus. Based on the Markov chain Monte Carlo sampling,  $L_c$  is bounded between 12 m and 4.8 km at 95% confidence. The largest values, corresponding to unrealistically large  $d_c$ , are close to the circumference of the ring fault. In this case the expression for the critical nucleation length should be modified to account for slip on a curved fault and interaction with the magma reservoir. For the smaller  $L_c$ , accelerating slip would have ruptured both vertically and laterally around the ring fault.

The improved understanding of caldera collapse mechanics could ultimately lead to improved forecasts of collapse onset and evolution. Our results demonstrate that laboratory-derived friction laws and constitutive parameters determined by small-scale experiments are completely consistent with unstable stick-slip on shallow faults at the kilometer scale. This provides more confidence in rate-state friction modeling in other contexts including tectonic faulting and human-induced seismicity.

## **Materials and Methods**

Conservation of mass of magma within the reservoir is 
$$\frac{d}{dt} \int_{V} \rho(x,t) dV = \int_{V} \frac{d}{dt} \rho(x,t) dV + \int_{S} \rho(x,t) \mathbf{v}_{t} \cdot \mathbf{n} \ dS = -q, \qquad \textbf{[6]}$$

where x and t are position and time, V is the reservoir volume with surface S,  $\rho$  is magma density,  $\mathbf{v}_t \cdot \mathbf{n}$  gives the outward velocity of the reservoir boundary, and -q is the mass flux out of the chamber. We separate the velocity of the boundary into elastic and inelastic components,  $\mathbf{v}_t = \mathbf{v}_e + \mathbf{v}_t$ where  $\mathbf{v}_{e}$  is the elastic component. The inelastic displacement is dominated by roof collapse such that the contribution to the surface integral is approximately  $-\pi R^2 \rho v(t)$ , where v is the collapse velocity, the negative sign because downward block motion decreases the reservoir volume. Thus,

$$\int_{V} \frac{d}{dt} \rho(x, t) dV + \int_{S} \rho(x, t) \mathbf{v}_{e} \cdot \mathbf{n} \ dS - \pi R^{2} \rho v(t) \simeq -q.$$
 [7]

Neglecting spatial variations in density, the remaining integral over S can be approximated as  $\rho dV/dt = \rho V \beta_c dp/dt$ , where  $\beta_c \equiv (1/V)\partial V/\partial p$  is the chamber compressibility.

Linearizing the change in magma density in terms of its compressibility  $\beta$ , and assuming that compressibility varies only as a function of depth z, Eq. 7 reduces to

$$\rho \int_{z} A(z)\beta(z,t) \frac{dp(z,t)}{dt} dz + \rho V \beta_{c} \frac{dp}{dt} - \pi R^{2} \rho V(t) = -q,$$
 [8]

where A(z) is the depth-dependent cross-sectional area of the chamber. dp/dt is assumed independent of depth so that

$$\rho V(t)\bar{\beta}(t)\frac{dp}{dt} - \pi \rho R^2 V(t) = -q,$$
 [9]

where

$$\bar{\beta}(t) \equiv \frac{1}{V} \int_{z} A(z)\beta(z,t)dz + \beta_{c}(t)$$
 [10]

is the net compressibility; the first term is the depth-averaged magma compressibility.

The mass flux q depends on the pressure gradient driving flow, the viscosity of the magma, and the geometry of the conduit. For laminar flow in a conduit whose dimensions are insensitive to changes in pressure, q is proportional to the pressure difference between the outlet point in the magma chamber and the eruption site (Fig. 2). Gudmundsson et al. (17) assumed that the subsiding roof block fills the entire chamber cross-section such that the magmastatic head decreases as the block subsides. Their model did not include magma compressibility. In contrast, in ref. 15 the roof block occupies only a fraction of the chamber cross-section, such that the magmastatic head at the chamber outlet does not decline as the block descends. Here, we include both a changing magmastatic head and melt compressibility.

The chamber pressure, measured at the chamber top, in excess of the magmastatic head is  $p(t) - \rho g(L - \Delta h) - \rho gu(t)$ , where  $\Delta h$  is the initial height difference between the top of the caldera block and the eruption site, and ho gu accounts for the loss of pressure as the block displaces downward by u(t). Assuming the flux is proportional to this excess pressure, then

$$q = k \left[ p - \rho g(L - \Delta h) - \rho g u \right] = k \left[ p - p_e - \rho g u \right],$$
 [11]

where k depends on conduit geometry and melt viscosity and we define  $p_e \equiv \rho g(L - \Delta h)$ . Combining Eq. 11 with Eq. 9 leads to Eq. 2.

Model Limitations. The piston model assumes vertical ring faults whereas the faults at the surface are normal (inward dipping). Cocollapse deformations are consistent with normal faults that steepen to vertical at modest depth (23); however, this does not change the inferred pressure change significantly. Furthermore, SI Appendix, Fig. 2 shows that frictional parameters are not strongly correlated with collapse-induced pressure change, although b-a shows a weak dependence. Slip on inward-dipping faults should lead to an increase in fault normal stress, while the collapseinduced pressurization will cause a decrease in normal stress. Future studies that account for spatially resolved stresses on the ring fault and normalstress-dependent changes in state (37) will be required to address these auestions.

We have not included effects of dynamic weakening at high slip speed, such as "flash heating" (38, 39). Additional weakening can also arise

Downloaded at Diane Sullenberger on July 26, 2021

from thermal pressurization of pore fluids (40, 41), although this seems less likely for shallow faulting at Kīlauea due to the depressed water

**Steady-State Solution.** In the quasi-static limit,  $dv/dt \rightarrow 0$  in Eq. 1, and ignoring head loss as the block descends (the  $\rho gu$  term in Eq. 2), the governing equations (Eqs. 1-4) can be reduced to a second-order system in  $\nu$  and  $\theta$ . While the loss of magma head influences the long-term evolution of the eruption, it does not affect behavior on the time scale of several stick-slip cycles. Under these restrictions a steady-state slip speed  $v_{ss}$  exists if there are solutions to

$$\frac{R}{2L} \left( \rho_c g L - p_e \right) - \frac{\pi \rho R^3}{2kL} v_{ss} - \sigma \left[ f_0 + (a - b) \log \left( \frac{v_{ss}}{v^*} \right) \right] = 0.$$
 [12]

At steady state, pressurization of the magma due to the descending block is compensated by outflow from the reservoir. For steady-state velocity-strengthening friction (a-b>0) there is a single root,  $v_{ss}$ . With velocity-weakening friction (a - b < 0) there can be zero, one, or two roots

Nondimensionalization. It is useful to nondimensionalize the governing equations (Eqs. 1–4). We chose a characteristic length L, pressure  $p^* = \rho_c g L$ , and time  $t^* = \rho \beta_0 V_0/k$ , where 0 indicates initial values. The nondimensional system of equations thus becomes, where indicates nondimensional variables.

$$\mu \frac{d\hat{v}}{d\hat{t}} = \alpha (1 - \hat{p}) - \hat{\sigma}(f_0 + a \log \hat{v} + b \log \hat{\theta}/\hat{d}_c)$$
 [13a]

$$rac{d\hat{
ho}}{d\hat{t}} = -\Gamma(\hat{
ho} - \hat{
ho}_{
m e} - \gamma \hat{u}) + \kappa \hat{v}$$
 [13b]

$$\begin{split} \frac{d\hat{\rho}}{d\hat{t}} &= -\Gamma(\hat{\rho} - \hat{\rho}_{\rm e} - \gamma \hat{u}) + \kappa \hat{v} \\ \frac{d\hat{\theta}}{d\hat{t}} &= 1 - \frac{\hat{\theta}\hat{v}}{\hat{d}_{\rm c}} \end{split} \tag{13b}$$

$$\frac{d\hat{u}}{d\hat{x}} = \hat{v}.$$
 [13d]

Here, for simplicity we have used the conventional form for the friction coefficient, rather than the regularized form. Also,  $\hat{p} = p/p^*$ ,  $\hat{v} = vt^*/L$ ,  $\hat{\theta} = \theta/t^*$ ,  $\hat{d}_c = d_c/L$ ,  $\hat{u} = u/L$ . Eq. 13 represents a system of ordinary differential equations (ODEs), where the nondimensional parameters are

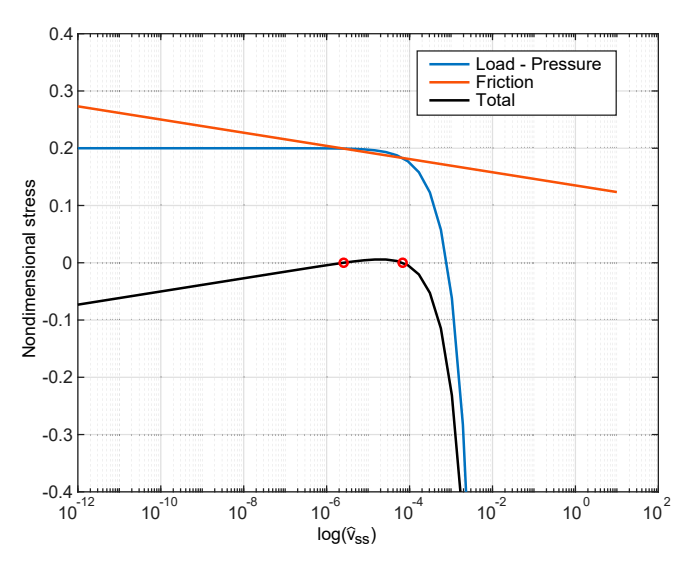


Fig. 6. Illustration of steady-state solutions. Black curve shows left hand side of Eq. 15 as a function of log v. Roots correspond to zero crossings (red circles). Blue and red curves show the nondimensional load minus pressure and shear resistance, respectively. Roots correspond to points where these curves cross.

$$\alpha = \frac{R}{2I}$$
 [14a]

$$\mu = \frac{R}{2qt^{*2}}$$
 [14b]

$$\Gamma = rac{V_0ar{eta}_0}{Var{eta}}$$
 [14c]

$$\gamma = \frac{\rho}{\rho_c}$$
 [14d]

$$\kappa = \frac{\pi R^2}{\rho q \bar{\beta} V}$$
 [14e]

$$\hat{\rho}_{e} = \frac{\rho}{\rho_{c}} \left( 1 - \frac{\Delta h}{L} \right).$$
 [14f]

Linearized Stability Analysis. For a stable limit cycle to exist in a secondorder system there must be a fixed point (Poincaré-Bendixson theorem). In the quasi-static limit,  $\mu d\hat{v}/dt \ll 1$ , and ignoring the head loss as the block descends (setting  $\gamma={\bf 0}{\bf )}$  the governing Eq. 13 can be reduced to a second-order system in  $(\hat{v}, \hat{\theta})$ . The nondimensional form of Eq. 12 is

$$\alpha(1 - p_e - \frac{\kappa}{\Gamma} \hat{v}_{ss}) - \hat{\sigma} [f_0 + (a - b) \log(\hat{v}_{ss})] = 0.$$
 [15]

For steady-state velocity-strengthening friction (a - b > 0) there is a single root,  $\hat{v}_{ss}$ . With velocity-weakening friction (a – b < 0) if the first term, the normalized load minus pressure, is less than steady-state shear stress for all  $\hat{v}_{ss}$ , then there are no steady-state solutions. Otherwise, there can be either one or two roots (Fig. 6). Note that the slope of Eq. 15 with respect to  $\hat{v}_{ss}$ 

$$S \equiv \frac{\hat{\sigma}(b-a)}{\hat{v}_{ss}} - \frac{\alpha \kappa}{\Gamma}$$
 [16]

is positive at the lower root and negative at the upper root. If  $\mathcal{S}\,{=}\,0$  and Eq. 15 is satisfied, there is a single root  $\hat{v}_{ss} = \hat{\sigma}(b-a)\Gamma/\alpha\kappa$ . At the lowerspeed root the steady-state friction decreases with increasing  $v_{ss}$  faster than the stress required to maintain force balance, suggesting that this root is unstable. At the higher-speed root the required stress decreases faster than steady-state frictional resistance; this root is thus expected to be conditionally unstable.

We seek solutions to the governing equations linearized around steady state, assuming one exists, of the form est, equivalent to finding the eigenvalues of the systems of ODEs. This leads to a characteristic equation

$$\hat{\sigma}as^{2} + \left[ \left( \alpha \kappa - \frac{\hat{\sigma}(b-a)}{\hat{d}_{c}} \right) v_{ss} + \hat{\sigma}a\Gamma \right] s - S \frac{\hat{v}_{ss}^{2}\Gamma}{\hat{d}_{c}} = 0.$$
 [17]

Note that  $\kappa$  plays a role similar to spring stiffness in the classic spring-slider model (3). However,  $\hat{v}_{ss}$  is a function of  $\kappa$ , making  $\kappa$  an inappropriate independent variable;  $\hat{d}_c$  is thus preferable as the independent variable in the stability analysis. For a single steady-state solution  $\mathcal{S}=0$ ; the solution to Eq. 17 in the limit that  $\hat{d}_c \to \infty$  is  $s \to -\Gamma b/a < 0$ , making the system stable. However, as  $\hat{d}_c$  decreases s will become positive (and real) and solutions unstable. The single solution s crosses into the real half-plane along the real axis, when

$$(\hat{d}_c)_{crit} = \frac{\hat{\sigma}(b-a)^2}{\alpha b \kappa}.$$
 [18]

This critical value determines whether small perturbations smoothly decay  $[\hat{d}_c > (\hat{d}_c)_{crit}]$  or grow  $[\hat{d}_c < (\hat{d}_c)_{crit}]$ .

Next, consider the case where there are two steady-state solutions. In the limit that  $\hat{d}_c \rightarrow \infty$ , Eq. 17 reduces to

$$\hat{\sigma}as^{2} + (\alpha\kappa\hat{v}_{ss} + \hat{\sigma}a\Gamma)s - S\frac{\hat{v}_{ss}^{2}\Gamma}{\hat{d}_{c}} = 0.$$
 [19]

For the higher-speed steady-state solution, for which S < 0,  $\Re(s) < 0$  for both roots, meaning this system is stable to small perturbations in this limit. However, for the lower-speed steady-state solution for which S > 0,  $\Re(s) > 0$ for one root such that the system is unstable to small perturbations even for

Restricting attention to the higher-speed steady-state solution  $\hat{v}_{ss}$ , note that s = 0 is not a solution to Eq. 17. Thus, as  $\hat{d}_c$  decreases the roots must cross into the real half-plane as a complex conjugate pair, corresponding to a Hopf bifurcation. Let  $s=\pm i\omega$  and set the real and imaginary parts of Eq. 17 to zero separately. The imaginary part leads to

$$(\hat{d}_c)_{crit} = \frac{\hat{\sigma}(b-a)}{\alpha\kappa + \hat{\sigma}a\Gamma/\hat{v}_{ss}}.$$
 [20]

Numerical results confirm that for  $\hat{d}_c > (\hat{d}_c)_{crit}$  small perturbations from the upper steady-state solution are damped, while for  $\hat{d}_c < (\hat{d}_c)_{crit}$  they grow. In contrast, perturbations around the lower speed  $\hat{v}_{ss}$  are unstable. Making this result dimensional leads to Eq. 5.

**Numerical Methods.** The nondimensional equations (13) are integrated using ode15s in MATLAB. If this solver is unable to achieve the requested accuracy or the solution is too slow, the code automatically switches to ode23s. This integrates until either a specified number of stick–slip cycles is achieved (typically 4) or the solution reaches steady state or magmastatic conditions. Roughly 300 sample runs of 2.2 million (0.014%) failed to adequately converge in the allotted time and are eliminated from the results. Initial conditions are chosen as follows: From a nondimensional velocity of  $10^{-4}$  and a shear stress slightly above steady state,  $\theta$  is computed from the friction law, and nondimensional pressure is computed from the momentum balance without inertia. If the initial

- J. H. Dieterich, Potential for geophysical experiments in large scale tests. Geophys. Res. Lett. 8, 653–656 (1981).
- B. S. Wu, G. C. McLaskey, Contained laboratory earthquakes ranging from slow to fast. J. Geophys. Res. Solid Earth 124, 10270–10291 (2019).
- A. Ruina, Slip instability and state variable friction laws. J. Geophys. Res. 88, 10359– 10370 (1983).
- C. Marone, Laboratory-derived friction laws and their application to seismic faulting. Annu. Rev. Earth Planet. Sci. 26, 643–696 (1998).
- N. Lapusta, Y. Liu, Three-dimensional boundary integral modeling of spontaneous earthquake sequences and aseismic slip. J. Geophys. Res. 114, B09303 (2009).
- K. L. Allison, E. M. Dunham, Earthquake cycle simulations with rate-and-state friction and power-law viscoelasticity. *Tectonophysics* 733, 232–256 (2018).
- P. G. Okubo, J. H. Dieterich, Effects of physical fault properties on frictional instabilities produced on simulated faults. J. Geophys. Res. Solid Earth 89, 5817–5827 (1984).
- 8. H. Kanamori, E. E. Brodsky, The physics of earthquakes. *Rep. Prog. Phys.* **67**, 1429 (2004).
- M. Cocco, A. Bizzarri, On the slip-weakening behavior of rate-and state dependent constitutive laws. Geophys. Res. Lett. 29, 11-1–11-4 (2002).
- S. M. Perry, V. Lambert, N. Lapusta, Nearly magnitude-invariant stress drops in simulated crack-like earthquake sequences on rate-and-state faults with thermal pressurization of pore fluids. J. Geophys. Res. Solid Earth 125, e2019JB018597 (2020).
- A. M. Rubin, J.-P. Ampuero, Earthquake nucleation on (aging) rate and state faults. J. Geophys. Res. 110, B11312 (2005).
- Y. Guglielmi, F. Cappa, J.-P. Avouac, P. Henry, D. Elsworth, Seismicity triggered by fluid injection-induced aseismic slip. Science 348, 1224–1226 (2015).
- P. Bhattacharya, R. C. Viesca, Fluid-induced aseismic fault slip outpaces pore-fluid migration. Science 364, 464–468 (2019).
- F. Cappa, M. M. Scuderi, C. Collettini, Y. Guglielmi, J.-P. Avouac, Stabilization of fault slip by fluid injection in the laboratory and in situ. Sci. Adv. 5, eaau4065 (2019).
- H. Kumagai, Very-long-period seismic signals and caldera formation at Miyake Island, Japan. Science 293. 687–690 (2001).
- L. Michon, N. Villeneuve, T. Catry, O. Merle, How summit calderas collapse on basaltic volcanoes: New insights from the April 2007 caldera collapse of Piton de la Fournaise volcano. J. Volcanol. Geoth. Res. 184, 138–151 (2009).
- M. T. Gudmundsson et al., Gradual caldera collapse at Bárdarbunga volcano, Iceland, regulated by lateral magma outflow. Science 353, aaf8988 (2016).
- O. Roche, T. H. Druitt, Onset of caldera collapse during ignimbrite eruptions. Earth Planet Sci. Lett. 191, 191–202 (2001).
- T. H. Druitt, R. S. J. Sparks, On the formation of calderas during ignimbrite eruptions. Nature 310, 679–681 (1984).
- K. R. Anderson et al., Magma reservoir failure and the onset of caldera collapse at Kilauea volcano in 2018. Science 366, eaaz1822 (2019).
- C. A. Neal et al., The 2018 rift eruption and summit collapse of Kilauea volcano. Science 363, 367–374 (2019).

pressure is less than  $p_e$  (in which case magma would flow into the chamber), the model is rejected.

The model predictions are computed from the results of the ODE solver as follows: 1) The first stick–slip event is discarded, as it is strongly influenced by initial conditions; 2) the cycle time is the median of the time between peaks; 3) the duration of stick–slip events is defined as the median time during which slip speed exceeds 0.1 m/s in each cycle; 4) the pressure change is the difference between the median of pressure maxima and that of pressure minima; 5) the slip per event is the median of the difference in cumulative slip at the times of peak velocity; 6) the peak stress, taken to be the frictional strength, is the median of the peak in the product of the rate–state friction and the effective normal stress; and 7) the decay time is found by fitting the last complete cycle with an exponential decay using Isqcurvefit.

**Data Availability.** Previously published data were used for this work [Segall et al. (23)].

ACKNOWLEDGMENTS. We thank Robert Viesca, Allan Rubin, Eric Dunham, and Taiyi Wang for discussions. Comments from Nick Beeler and two anonymous reviewers significantly improved the manuscript. GPS data are available from the UNAVCO archive (https://www.unavco.org/data/data.html). Any use of trade, firm, or product names is for descriptive purposes only and does not imply endorsement by the US Government.

- D. R. Shelly, W. A. Thelen, Anatomy of a caldera collapse: Kilauea 2018 summit seismicity sequence in high resolution. Geophys. Res. Lett. 46, 14395–14403 (2019).
- P. Segall, K. R. Anderson, F. Pulvirenti, T. Wang, I. Johanson, Caldera collapse geometry revealed by near-field GPS displacements at Kilauea volcano in 2018. Geophys. Res. Lett. 47, e2020GL088867 (2020).
- J. R. Rice, N. Lapusta, K. Ranjith, Rate and state dependent friction and the stability
  of sliding between elastically deformable solids. J. Mech. Phys. Solid. 49, 1865–1898
  (2001).
- 25. R. M. Iverson, Dynamics of seismogenic volcanic extrusion at Mount St. Helens in 2004-05. *Nature* **444**, 439-443 (2006).
- A. Roman, P. Lundgren, Dynamics of large effusive eruptions driven by caldera collapse. Nature 592, 392–396 (2021).
- S. Owen, Rapid deformation of Kilauea volcano: Global positioning system measurements between 1990 and 1996. J. Geophys. Res. 105, 18983–18998 (2000).
- R. P. Denlinger, J. K. Morgan, "Instability of Hawaiian volcanoes" in USGS Professional Paper, M. P. Poland, T. J. Takahashi, C. M. Landowski, Eds. (US Geological Survey, 2014), vol. 1801, pp. 149–176.
- L. Zhang, C. He, Y. Liu, J. Lin, Frictional properties of the South China Sea oceanic basalt and implications for strength of the Manila subduction seismogenic zone. *Mar. Geol.* 394, 16–29 (2017).
- H. Munekane, J. Oikawa, T. Kobayashi, Mechanisms of step-like tilt changes and very long period seismic signals during the 2000 Miyakejima eruption: Insights from kinematic GPS. J. Geophys. Res. Solid Earth 121, 2932–2946 (2016).
- N. Lapusta, Y. Liu, Three-dimensional boundary integral modeling of spontaneous earthquake sequences and aseismic slip. J. Geophys. Res. Solid Earth 114, B09303 (2009)
- A. Hackston, E. Rutter, The Mohr–Coulomb criterion for intact rock strength and friction—A re-evaluation and consideration of failure under polyaxial stresses. Solid Earth 7, 493–508 (2016).
- R. A. Schultz, Brittle strength of basaltic rock masses with applications to Venus. J. Geophys. Res. Plan 98, 10883–10895 (1993).
- M. Patrick, T. Orr, K. Anderson, D. Swanson, Eruptions in sync: Improved constraints on Kilauea volcano's hydraulic connection. Earth Planet Sci. Lett. 507. 50–61 (2019).
- J. R. Rice, J.-C. Gu, Earthquake after effects and triggered seismic phenomena. Pure Appl. Geophys. 121, 187–219 (1983).
- K. Yamaoka, M. Kawamura, F. Kimata, N. Fujii, T. Kudo, Dike intrusion associated with the 2000 eruption of Miyakejima volcano, Japan. Bull. Volcanol. 67, 231–242 (2005).
- M. F. Linker, J. H. Dieterich, Effects of variable normal stress on rock friction: Observations and constitutive equations. J. Geophys. Res. 97, 4923–4940 (1992).
- N. M. Beeler, T. E. Tullis, D. L. Goldsby, Constitutive relationships and physical basis of fault strength due to flash heating. J. Geophys. Res. Solid Earth 113, B01401 (2008).
- 39. G. Di Toro et al., Fault lubrication during earthquakes. Nature 471, 494–498 (2011).
- 40. J. R. Rice, Heating and weakening of faults during earthquake slip. *J. Geophys. Res.* 111, B05311 (2006).
- R. C. Viesca, D. I. Garagash, Ubiquitous weakening of faults due to thermal pressurization. *Nat. Geosci.* 8, 875–879 (2015).

PNAS | 7 of 7